nature photonics

Article

https://doi.org/10.1038/s41566-024-01456-5

Atomic optical antennas in solids

Received: 21 August 2023

Accepted: 2 May 2024

Published online: 07 June 2024

Check for updates

Zixi Li[1,7], Xinghan Guo[1,7], Yu Jin[2], Francesco Andreoli[3], Anil Bilgin[1], David D. Awschalom[1,4,5], Nazar Delegan[1,5], F. Joseph Heremans[1,5], Darrick Chang[3,6], Giulia Galli[1,2,5] & Alexander A. High[1,5]

A resonantly excited atomic optical dipole simultaneously generates propagating (far) and evanescent (near) electromagnetic fields. The near-field component diverges in the limit of decreasing distance, indicating an optical antenna with the potential for enormous near-field intensity enhancement. In principle, any atomic optical dipole in a solid can serve as an optical antenna; however, most of them suffer from environmentally induced decoherence that largely mitigates field enhancement. Here we demonstrate that germanium vacancy centres in diamond—optically coherent atom-like dipoles in a solid—are exemplary antennas. We measure up to million-fold optical intensity enhancement in the near-field of resonantly excited germanium vacancies. In addition to the rich applications already developed for conventional nanoantennas, atomic antennas in the solid state promise to yield interesting new applications in spectroscopy, sensing and quantum science. As one concrete example, we use germanium vacancy antennas to detect and control the charge state of nearby carbon vacancies and generate measurable fluorescence from individual vacancies through Förster resonance energy transfer.

Antenna-generated field confinement can be used to guide light and amplify light–matter interactions in a broad range of classical and quantum applications, including communications, sensing and imaging[1–3]. For applications in spectroscopy and chemistry such as single-molecule Raman spectroscopy or light-induced catalysis[4,5], the efficiency is directly correlated with the degree of field enhancement. A free atom or atom-like system could in principle have loss-free optical transitions and generate extreme enhancement to the field intensity at nanoscale lengths. Under resonant excitation, any atomic dipole will function as an antenna and create an evanescent near-field composed of high-wavevector (**K**-vector) light. At a distance R from a point-like dipole, the intensity of this evanescent field increases with decreasing distance ($\propto R^{-6}$) down to length-scales comparable with the size of the atomic orbitals[6]. However, this near-field enhancement is often limited by a number of environmentally induced non-radiative processes—including charge fluctuations, electromagnetic noise and phonon scattering—which are characterized by a non-radiative decay rate Γ'. These processes can be orders of magnitude stronger than the intrinsic radiative decay rate Γ_0, resulting in inhomogeneous optical broadening that severely limits the driving efficiency of atomic dipoles in solids.

Group IV colour centres in diamond are atomic defects characterized by exceptional optical coherence at low temperatures[7]. Composed of an interstitial group IV impurity ion and two carbon vacancies, group IVs possess D_{3d} group symmetry, which provides the optical transitions with first-order protection from electric field noise. Moreover, the symmetry leads to a high Debye–Waller factor, with relatively weak electron–phonon coupling and a high zero-phonon line (ZPL) emission rate[8]. Near-lifetime-limited transition linewidths have been observed for numerous group IVs so far, including the silicon (SiV)[9], germanium (GeV)[10] and tin (SnV) vacancy centres[11].

Numerical analysis of the scattered field of a resonantly excited GeV reveals its potential as an atomic antenna for giant local field

[1]Pritzker School of Molecular Engineering, University of Chicago, Chicago, IL, USA. [2]Department of Chemistry, University of Chicago, Chicago, IL, USA. [3]ICFO – Institut de Ci'encies Fotòniques, The Barcelona Institute of Science and Technology, Castelldefels, Spain. [4]Department of Physics, University of Chicago, Chicago, IL, USA. [5]Center for Molecular Engineering and Materials Science Division, Argonne National Laboratory, Lemont, IL, USA. [6]ICREA—Institució Catalana de Recerca i Estudis Avançats, Barcelona, Spain. [7]These authors contributed equally: Zixi Li, Xinghan Guo.
e-mail: ahigh@uchicago.edu

https://doi.org/10.1038/s41566-024-01456-5

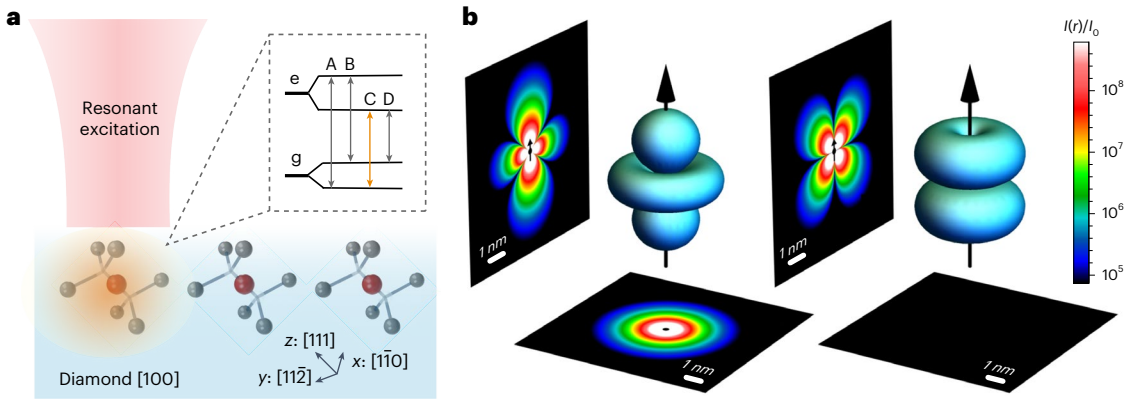

Fig. 1 | The GeV as an antenna. a, A schematic showing that while under resonant excitation, a GeV can function as an antenna with a strongly enhanced evanescent near-field. **b**, Electromagnetic field enhancement of the GeV, assuming illumination by a resonant input field (C-line in **a**) that is polarized along the GeV dipole axis (*z*-direction in **a**). The 3D contours represent cases in which $I(r)/I_0 = 5 \times 10^5$. The left (right) surface corresponds to the near-field polarized along (perpendicular to) the GeV dipole orientation. The density plots (left and bottom) show the intensity of the total scattered field as a function of distance.

enhancement. A schematic of a GeV is depicted in Fig. 1a. In this work we focus on the C-line ZPL transition between the lower ground and excited states (Fig. 1a, inset). Further information on the other three transitions (A, B, D) can be found in ref. 12. To model the field profile of a resonantly excited GeV, our calculation assumes a homogeneous broadening of ~3 times the GeV natural linewidth, which is comparable with our measurements and reported values[9,13,14]. Figure 1b shows the computed scattered optical field intensity of the GeV as a function of distance and angle, assuming resonant illumination with polarization aligned with the dipole orientation (that is, the *z*-direction in Fig. 1a). Notably, the scattered field can become much more intense than the resonant excitation field, with the enhancement in intensity reaching magnitudes of $\gtrsim 10^8$ at distances of $\lesssim 1$ nm (see Supplementary Section 1 for details). Such atomic antennas offer distinct opportunities compared with existing nanoantennas. First, being a molecule with quantum mechanical properties, the antenna itself provides a unique platform. Second, as a point-like quantum emitter with a low non-radiative decay rate, it can manifest field enhancements and scattering cross-sections that are essentially decoupled from its physical size, leading to the remarkable enhancements mentioned above. This stands in contrast to small metallic scatterers whose response inherently diminishes with decreasing particle size due to Ohmic losses[15,16]. Finally, the very narrow linewidth of the GeV (compared with usual nanoantennas) provides a remarkable sensitivity to perturbations of the resonance frequency.

In this study we leverage the unique antenna properties of GeVs to both detect and manipulate nearby carbon monovacancies (V_C). We observe the V_C charge state cycling through energetic splitting and hopping in the GeV ZPL. Combining antenna sensitivity and field enhancement, we resonantly manipulate the charge state of the V_C. We also use GeV antennas and Förster resonance energy transfer (FRET) to drive detectable fluorescence from individual neutral vacancies (GR1 centres; see below) for the first time. By comparing V_C charge cycling for far-field driving and on-resonant excitation of a local GeV, we demonstrate an up to one-million-fold intensity enhancement in the GeV near-field. The magnitude of the intensity enhancement at the V_C strongly correlates with the Stark-shift-induced transition splitting and hence V_C-to-GeV separation, underscoring the pronounced near-field characteristics of the process. We also explore the distinctions between GeV antenna properties and those of conventional antennas. To conclude, we discuss applications and future research directions of atomic antennas across a broad range of scientific disciplines.

Experimental study of GeV antennas

We study GeV antennas through their optical and electronic interactions with local V_C. We first demonstrate that the GeV ZPL acts as a charge state sensor for proximal carbon monovacancies. Although the GeV is symmetry-protected from first-order direct current Stark effects[8], charges localized within a few nanometres of the GeV can generate measurable second-order Stark shifts in the ZPL. We use density functional theory (DFT) to calculate these shifts as a function of electric field direction and GeV–charge separation (Fig. 2a; refer also to Supplementary Section 3 for more details). Our calculations reveal that charges within 4 nm create Stark shifts that exceed 0.5 GHz. Consequently, charge state transitions in nearby defects will induce a corresponding hopping of the GeV ZPL between discrete, energetically split transitions. In agreement with past reports[14,17,18], we commonly observe this phenomenon in GeVs when using resonant photoluminescence excitation (PLE) (Fig. 2b), with the observed splitting ranging from 0.3 GHz to 17 GHz. Through a comprehensive experimental study and the systematic elimination of other potential sources (including the Jahn–Teller effect in the presence of strain, and hydrogen reorientation near GeVs), we attribute this phenomenon to proximal carbon monovacancies undergoing charge state transitions between V_C^0 (GR1) and V_C^- (ND1) (Supplementary Section 4). The primary evidence of their individual nature lies in the discrete, two-level GeV PLE spectrum, in contrast to random spectral diffusion occurring from ensembles of noise sources.

The combination of near-field optical intensity enhancement and charge sensitivity of the GeV antenna allows us to resonantly manipulate V_C charge states. Under far-field optical illumination, the V_C can cycle between the neutral and negatively charged state[19–21], analogous to charge cycling commonly observed in other semiconductor defects[22,23]. Alternatively, the intense optical near-field in proximity to a resonantly illuminated GeV can provide a local energy source to drive charge cycling (Fig. 2c). To demonstrate this interaction, we employ a continuous-wave laser pump tuned to multiple frequencies (resonant, partially resonant and off-resonant) with respect to the two split GeV ZPL frequencies (denoted as C_1 and C_2). This is then followed in quick succession with a probe PLE scan across C_1 and C_2 (Fig. 2d). These results demonstrate that pumping one of the GeV ZPL peaks resonantly at C_1 (C_2) initializes the GeV ZPL at the other frequency C_2 (C_1), corresponding directly to V_C photo-induced charge initialization through the GeV antenna. This can directly improve GeV spectral performance in quantum applications. For instance, one can resonantly pump the undesired ZPL peak (or peaks if multiple vacancies are around) when spectral hopping is present. Furthermore, by identifying vacancies as a source of spectral instability, this suggests GeV and other group IV colour centres can be stabilized by minimizing the local vacancy concentration; for example, through in situ doping, shallow implantation followed by overgrowth[24,25], or high-temperature annealing processes.

https://doi.org/10.1038/s41566-024-01456-5

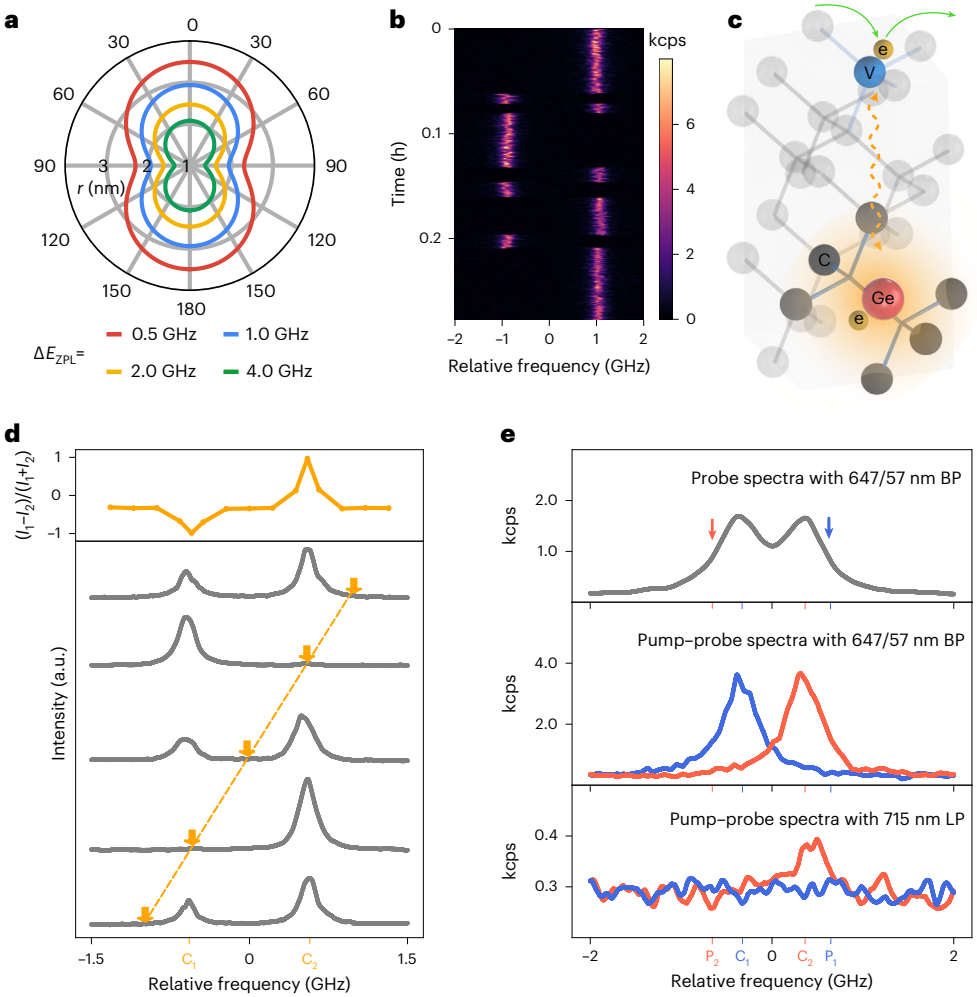

Fig. 2 | GeV antennas sense, manipulate and optically excite proximal vacancies. a, The Stark shift of a GeV's ZPL as a function of the distance to a nearby localized electron, and the electric field direction with respect to the GeV dipole axis, as calculated by DFT. **b**, Photoluminescence excitation spectrum of a GeV exhibiting spectral splitting and dynamic hopping over time. **c**, A schematic of a resonantly excited GeV provides a local energy source to drive the charge cycling in a proximal carbon vacancy. **d**, Average PLE spectra obtained at different pumping frequencies. The orange arrows in the lower figure indicate the pumping frequency, and each spectrum represents an average of 150 probe scans. The upper figure depicts the contrast between two ZPL peaks as a function of pumping frequency. **e**, Generation of photoluminescence from an individual GR1 using a GeV antenna. The upper figure displays an average PLE spectrum (grey) obtained from 200 probe scans without pumping. The blue/red PLE spectra in the middle and lower figures represent the average of 50 probe scans at the pumping frequency indicated by the blue/red arrow in the upper figure. The upper and middle spectra were measured using a 647/57 nm bandpass (BP) filter, while the lower spectra were measured using a 715 nm long-pass (LP) filter selective to the GR1 optical transition.

The prevalence of GeV hopping can also measure the local vacancy concentration and provide a useful metric for improving material quality.

Remarkably, we observe that, in addition to charge state control, GeV antennas can induce measurable photoluminescence from individual GR1s through FRET. In this process, the optical excitation of the GeV is directly transferred to the GR1, followed by GR1 fluorescence. Although FRET has previously been explored with nitrogen-vacancy centres in diamond, these studies utilized off-resonant, low-efficiency excitation through the phonon sideband[26,27]. Here we show that atomic-resonance-enhanced FRET can greatly improve the overall efficiency of the process and lead to a high signal-to-noise ratio even for weakly radiative systems. We investigate a GeV with two ZPL peaks, as shown in Fig. 2e. To optimize the initialization fidelity in the presence of peak overlap, we introduce a slight detuning to the two pumping frequencies (denoted P_1 and P_2), as shown in the upper and middle parts of Fig. 2e. By pumping the high-frequency peak of the GeV's ZPL (blue arrow, P_1), the V_C gains an electron. We next make use of wavelength filtering to selectively isolate GR1 photoluminescence at 730–850 nm from GeV and ND1 photoluminescence at 390–700 nm (Supplementary Section 5). Subsequent GeV excitation reveals an absence of a photoluminescence signal beyond 715 nm. Alternatively, pumping the low-frequency ZPL (red arrow, P_2) deionizes the V_C. In this condition, subsequent resonant GeV excitation creates measurable photoluminescence at the GR1 wavelength, as shown in the lower figure of Fig. 2e. This marks the first experimental observation of fluorescence from individual GR1s, which are challenging to resolve due to poor quantum efficiency and metastable shelving states[19]. Furthermore, these measurements confirm FRET between the GeV and V_C. The 3 nW probe power along with ~1 μm^2 beam size to observe single-vacancy FRET is several orders of magnitude lower than the typical powers (~10–100 $\mu W\ \mu m^{-2}$) used in comparable single-molecule FRET experiments[28,29]. The comparatively high overall FRET efficiency of GeV antennas, and corresponding high signal-to-noise for GR1 emission, directly originates from their excellent optical coherence and highlights their potential optical near-field explorations. Furthermore, the observation of state-dependent, wavelength-resolvable GR1 fluorescence further supports our model of charge cycling in proximal vacancies generating the observed GeV spectral splitting and hopping (Fig. 2b).

https://doi.org/10.1038/s41566-024-01456-5

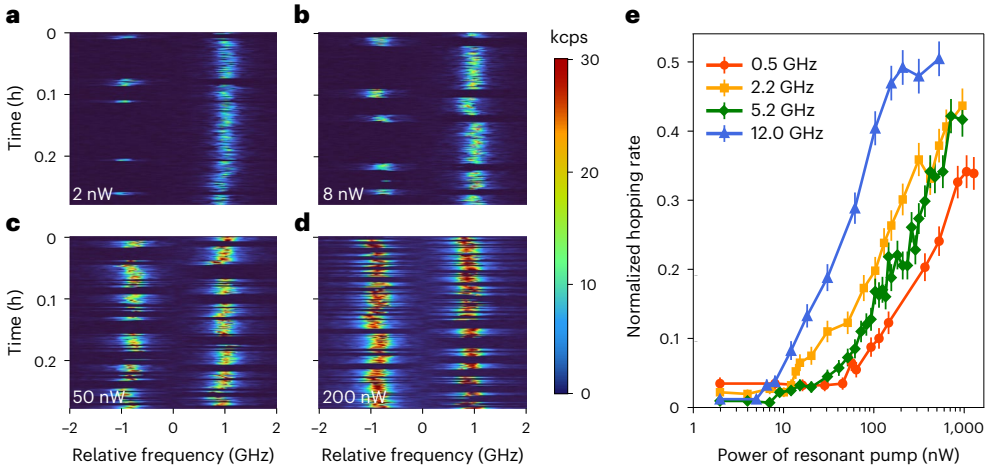

Fig. 3 | The ZPL splitting is inversely correlated with pumping threshold power. a–**d**, Time-dependent PLE spectra obtained at different excitation powers, at 2 nW (**a**), 8 nW (**b**), 50 nW (**c**) and 200 nW (**d**). The spectral hopping rate increases with higher probe powers. **e**, Normalized hopping rate of multiple GeVs with varying ZPL splitting magnitudes, plotted as a function of probe power. Data points are calculated as p/n, where p represents the proportion of '1' (indicating ZPL transitions) and n is the number of probe scans. Error bars are the s.d. of the estimated hopping rate, calculated as $\sqrt{p \times (1-p)/n}$ (ref. 49). The excitation power threshold decreases as the ZPL splitting magnitude increases.

We gain further insight into GeV antennas by examining the correlation between GeV–V_C separation, field intensity enhancement and the Stark shift. Both the strength of the Stark shift and antenna-induced optical interactions should decrease with increasing GeV–V_C separation (Figs. 1b and 2a). To quantify this trend, we repeatedly scan a continuous-wave laser across the two resonant frequencies of a hopping GeV; such scanning functions both as a pump to drive V_C charge state transitions and as a probe for the V_C charge state. The time-dependent PLE spectra of a GeV with a 2 GHz splitting magnitude (shown in Fig. 3a–d) reveal power-dependent dynamics in the adjacent V_C. Specifically, the PLE signal becomes brighter as the laser power increases from 2–8 nW (A to B), while the hopping rate remains unchanged. It is observed that further increasing the laser power above 50 nW (C and D) changes the hopping rate, indicating a threshold intensity for driving V_C charge cycling. To quantify the hopping rate, we define the normalized hopping rate as the frequency at which the ZPL switches to the opposite state from the previous scan, divided by the total number of probe scans (400 in all cases; Fig. 3e). We repeat these measurements for GeV with different ZPL splitting magnitudes, corresponding to a V_C–GeV separation of ~1–4 nm. The measurements (Fig. 3e) show that the threshold power (hopping rate) decreases (increases) as the splitting energy increases, signifying closer proximity between the V_C and GeV. This demonstrates the near-field nature of the optical intensity enhancement of the GeV antenna, which measurably diminishes over a few nanometres. We also note that we have observed GeVs with splitting magnitudes exceeding 15 GHz. However, in such cases, the V_C is situated too close to the GeV, potentially leading to orbital hybridization which can complicate the spectrum. Density functional theory analysis at these length-scales is currently under investigation and beyond the scope of this work.

We quantify the degree of near-field optical intensity enhancement by comparing V_C charge cycling under resonant pumping through the GeV antenna (as described in Fig. 3) and off-resonant pumping. We use a 633 nm (1.96 eV) laser for the off-resonant pump, which is far-red-detuned from the GeV resonance of 602 nm (2.06 eV) and cannot directly excite the GeV. The optical set-up and laser sequences are detailed in Fig. 4a. In Fig. 4b we present the power-dependent hopping rate of a GeV with a ZPL splitting of 12 GHz, using both resonant and off-resonant pump methods. We observe a substantial difference spanning ~3–4 orders of magnitude in the threshold laser power between resonant and off-resonant pumps. We also study the hopping rate with a continuous-wave pump 0.01 nm detuned from the transition, revealing the hopping rate remains unchanged even when the slightly detuned pump reaches its maximum power (~1 µW). These measurements confirm that although resonant excitation of the GeV creates a local enhancement of the optical field, no such enhancement exists in the off-resonance regime.

Our investigations for on- and off-resonance pumping reveal that the GeV antenna generates up to million-fold optical intensity enhancement at proximal carbon monovacancies. We note that the resonant excitation involves laser scanning across the resonance frequency in a linear pattern, with a much larger scanning range (15 GHz) than the ZPL linewidth. As a result, only a narrow range of frequencies in the scan effectively drive the GeV. Furthermore, the dwell time of each scanning step is at the millisecond level, while off-resonant driving necessitates a pumping duration of seconds to achieve comparable hopping rates. To accommodate this frequency- and duration-dependent pumping, we use pump fluence to characterize the hopping threshold, which for resonant excitation is a combined function of the laser power as well as the scanning speed and the ZPL lineshape (see Methods for details). The threshold fluence for resonant GeV excitation correlates inversely with the magnitude of ZPL splitting, while no such correlation exists for far-field V_C excitation (Fig. 4c). Indeed, far-field-driven V_C charge cycling rates are highly similar across our measurements (see Supplementary Section 5 for more details). By comparing the threshold fluences, we derive the field enhancement at the V_C generated by the GeV antennas, as shown in Fig. 4d. The results indicate that GeV antennas create field intensity enhancement at nearby vacancies spanning orders of magnitude from 10^4 to 10^6. We note that the experimental values of field enhancement are slightly lower than the theoretical calculations presented in Fig. 1b, which can be partially attributed to suboptimal factors such as the polarization of the input field and the observation angle in space. Nonetheless, the observed intensity enhancements firmly establish GeV as an outstanding optical antenna.

Comparison with conventional nanoantennas

With these experimental values on hand, we conduct an analytical comparison between GeV optical antennas and conventional plasmonic antennas. We begin by recalling the relevant properties of the GeV. First, akin to any point-like dipolar resonance, its near-field enhancement at a distance R follows $|E_{max}(R)/E_0|^2 \simeq 9(1+\sigma_{abs}/\sigma_{sc})^{-2}(k_0R)^{-6}$, where the numerical pre-factor assumes an optimal angle of

https://doi.org/10.1038/s41566-024-01456-5

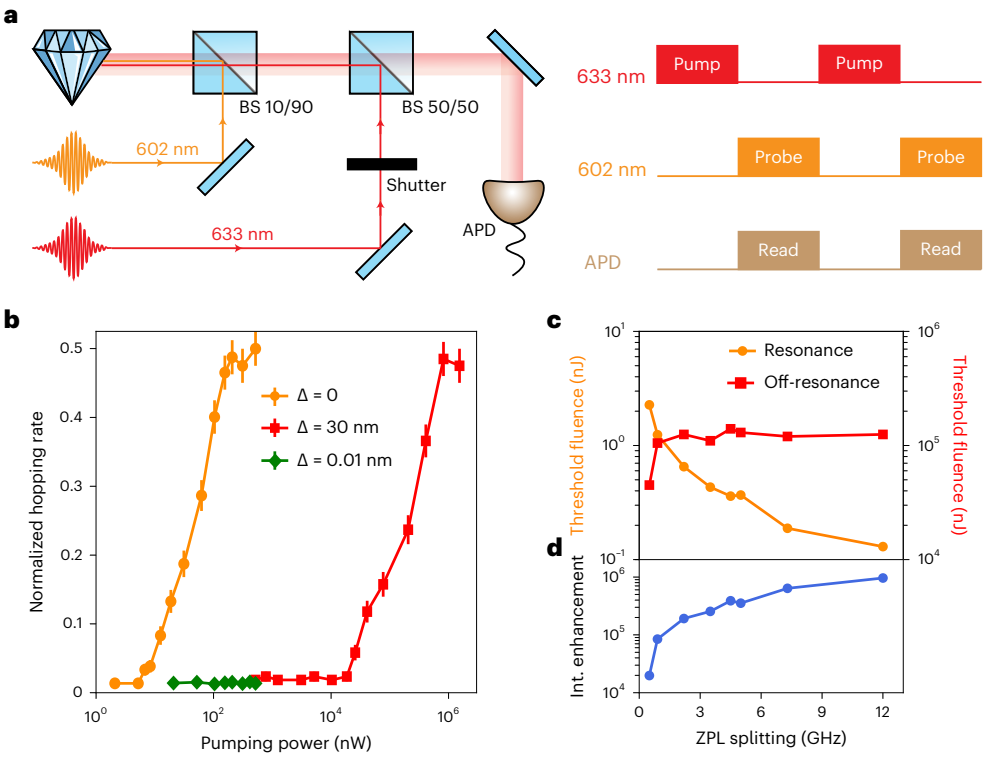

Fig. 4 | Comparison with off-resonant excitation reveals field enhancement. **a**, Optical set-up and laser sequences for off-resonant pump measurements. BS, beamsplitter; APD, avalanche photodetector. Each pump, probe and readout lasts 5 s. We maintain the probe power at the low level of 3 nW throughout the measurements to mitigate probe-induced hopping. **b**, Normalized hopping rates of a GeV with a ZPL splitting of 12 GHz, with varying pump frequencies, plotted as a function of pump power, where Δ represents the detuning from GeV's resonance. Data points are calculated as p/n, where p represents the proportion of '1' (indicating ZPL transitions) and n is the number of probe scans. Error bars are the s.d. of the estimated hopping rate, calculated as $\sqrt{p \times (1-p)/n}$. **c**, Threshold of resonant pump fluence and off-resonant pump fluence, displayed as a function of GeV's ZPL splitting magnitude. From each hopping rate curve, we define a threshold pump power as the power at which the hopping rate increases to 1.5 times the hopping rate at the previous power level. We then calculate the corresponding threshold pump fluence by multiplying the pump power by the effective pump duration. **d**, Derived optical field enhancement from the GeV antenna versus GeV's ZPL splitting magnitude.

observation. In this equation, the ratio between the scattering (σ_{sc}) and absorption (σ_{abs}) cross-sections quantifies the ability to drive the nano-antenna[30]. Notably, for a GeV, this ratio $\sigma_{sc}/\sigma_{abs} = \Gamma_0/\Gamma'$ is decoupled from its physical size, and the $\propto (k_0 R)^{-6}$ scaling persists down to distances of $\lesssim$1 nm, owing to the small size of the GeV. Furthermore, the total linewidth of the GeV (given by $\Gamma_0 + \Gamma' \approx 4\Gamma_0 \approx 2\pi \times 100$ MHz) can be extremely narrow. Importantly, the combination of high optical intensity (over nanometric scales) and fine spectral bandwidth has been a key factor in the experimental detection and manipulation of the charged state of neighbouring vacancies.

We now compare these properties with a paradigmatic dipolar nanosystem, namely, a metallic nanosphere with a radius $k_{in}R \ll 1$, where k_{in} is the wavevector of the input light (in the visible spectrum). Despite considering this specific and simple system, we also highlight aspects of these results that are rather general. When driven at its resonant frequency, the maximum field enhancement of the nanosphere follows the same equation as the GeV (due to the analogous, that is, electric-dipolar, response) down to a minimum distance given by its radius, which we assume to be equivalent to the value of R for the purpose of establishing a proper comparison. Nonetheless, now the key ratio $\sigma_{sc}/\sigma_{abs} = 2(k_{in}R)^3 Q/3$ exhibits a linear decrease as the volume of the nanosphere decreases, with a proportionality constant set by the quality factor Q of the material (Supplementary Section 2). This implies a detrimental suppression of the antenna response at small R, eventually balancing the $\propto (k_{in}R)^{-6}$ scaling and limiting the field enhancement to $|E_{max}/E_0|^2 \approx 500$ (given the best-case scenario of silver). More generally, the scattering cross-section of any lossy nanoparticle must fundamentally decrease—at least linearly—with the volume[15]. At the same time, their linewidth should generally be affected by the relatively low Q of the material, resulting in a very large linewidth compared with that of the GeV; for the specific case of a silver nanosphere, this can be quantified as ~$2\pi \times 10$ THz.

As represented in Fig. 5a, the subwavelength $k_{in}R \ll 1$ prediction (black, dashed line) represents an upper bound to the field enhancement of the nanosphere as a function of the radius R (ref. 31), as confirmed by the blue points calculated through the full Mie theory[32,33] (Supplementary Section 2). Remarkably, when $R \lesssim 20$ nm, the GeV exhibits a much stronger intensity enhancement. Moreover, even in the presence of stronger non-radiative and inelastic processes of up to $\Gamma' = 300\Gamma_0$, the field intensity remains greatly enhanced within 5 nm. Overall, this must be attributed to the improved value of σ_{sc}/σ_{abs}, as shown in Fig. 5b.

To complete the comparison, we consider the temperature dependence of non-radiative losses (Γ') of the GeV, which sharply increases at temperatures higher than those of our experimental set-up (4 K) due to phonon scattering. In Fig. 5c we predict how the field enhancement would be modified as a function of T, using the experimental data from refs. 10,34 to estimate $\Gamma'(T)$. We compare the maximum near-field at distances R (nm) = 0.5, 1, 2, 5 from the GeV (solid, coloured lines) with that of a silver nanosphere (black, dashed line). Beyond the concrete example of a nanosphere, in the figure we also plot the maximum near fields associated with other common nanoantennas[35–39] (grey-to-white-shaded region; see Supplementary Section 2 for details). Again, the GeV exhibits excellent performance by

https://doi.org/10.1038/s41566-024-01456-5

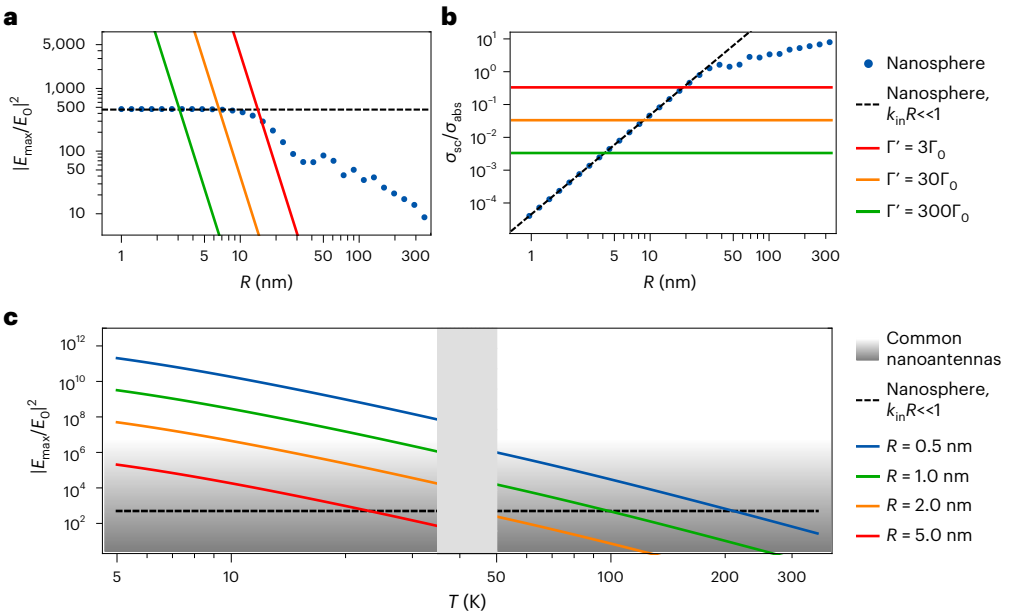

Fig. 5 | The antenna effect of a GeV compared with a silver nanosphere. **a**,**b**, The solid, coloured lines show either the maximum, near-field enhancement (**a**) or the ratio σ_{sc}/σ_{abs} between the scattering and absorption cross-sections (**b**), as a function of the distance R (in nanometres) from the GeV. The red, orange and green colours are related to different values of the non-radiative rate $\Gamma'/\Gamma_0 = 3, 30, 300$. As a comparison, the blue points show the theoretically calculated values for a silver nanosphere of radius R, illuminated at the resonant condition $\lambda_{in} = 354$ nm, which guarantees the maximum field enhancement[50]. This is calculated by a full Mie expansion, up to the first 15 multipole orders[51]. By contrast, the black dashed lines show the quasi-static limit of the nanosphere, which is valid for a subwavelength radius $k_{in}R \ll 1$ (ref. 6). **c**, Expected enhancement of the near-field by a GeV, as a function of the temperature T. Different colours are related to fields observed at different distances R (nm) = 0.5, 1, 2 or 5 from the colour centre. The data for $\Gamma'(T)$ are taken from ref. 34 for low temperatures ($T \lesssim 35$ K) and from ref. 10 for high temperatures ($T \gtrsim 50$ K). The grey-to-white-shaded region depicts the usual range of field enhancements by common plasmonic nanoantennas[35–39].

comparison, at least at cryogenic temperatures; however, at temperatures exceeding ~50 K, only at small distances of $\lesssim$1 nm is the GeV response expected to remain higher or comparable with nanospheres. This prompts the development of atomic antennas with reduced phonon interactions[40], aiming for room-temperature investigations.

Discussion

Our study reveals the remarkable capability of atomic defects in solids to concentrate optical energy, and sense and manipulate their proximal environment. This discovery could impact a broad range of scientific disciplines. Atomic antennas can be used in nanoscale volume explorations of Raman spectroscopy, FRET-based detection schemes and photochemistry. Crucially, unlike plasmon-based processes, GeV antennas are nearly loss-free and only require nanowatts of power to efficiently drive near-field processes. This ultra-low power can mitigate the detrimental photobleaching, heating processes and background fluorescence that are common in single-molecule Raman and FRET spectroscopy. The demonstrated sensitivity to, and control of, local, individual charges (unlike conventional plasmonic antennas) enables dynamical optical studies of single-electron processes in chemistry and materials. Near-surface group IV colour centres maintain excellent optical coherence, as demonstrated in nanodiamonds[9], indicating that GeV antennas can optically study and manipulate processes at the diamond surface, broadening the range of potential sensing and interaction targets and adding a new dimension to diamond-based quantum sensing. Whereas surface-enhanced Raman spectroscopy and other advanced plasmonic methods rely on carefully tailored plasmonic surfaces and cavities for intensity enhancement, the antenna studies here are intrinsically simple in structure, composed of a single vacancy and single impurity atom. Advanced diamond material methods, such as delta-doping, patterned implantation and optical colour centre generation can be leveraged to control the placement of GeV antennas co-localized with targets[25,41,42]. Furthermore, although a plasmonic system is essentially classical, the GeV is intrinsically a quantum emitter that can only interact with a single photon at a time, which may prompt the development of new theories and enable additional capabilities. Furthermore, group IV colour centres are commonly used in cavity quantum electrodynamics experiments and can have highly probabilistic spin–photon interactions in nanophotonic structures[43]. In these experiments, spectral stability is necessary for photon-based entanglement schemes. We show a pathway to initialize and stabilize GeV emission even in the presence of charge defects. Finally, we emphasize that for optical atomic antennas in solids, the primary metric for optical intensity enhancement is the relative strength of elastic radiative emission rate compared with other emission mechanisms (see Supplementary Section 1 for details). Highly coherent optical transitions have been observed in several systems, including molecules, defects in hexagonal boron nitride and silicon carbide, and rare-earth dopants[44–48]. This suggests considerable flexibility in the integration and study of atomic or molecular antennas and prompts investigation in a broad range of solids. For example, incorporating atomic antennas into van der Waals heterostructures can facilitate the study and manipulation of electronic processes. Furthermore, targeted binding of optically coherent molecules to specific chemical structures can enable nanoscale probing and manipulation of the target system[47,48]. Certainly, conventional antennas can be engineered over a broad range of design parameters, beyond those emphasized for the GeV here. It would be intriguing to explore the extent to which more flexible atomic antennas can be realized, for example, by investigating whether ensemble atomic antennas could be positioned with nanoscale precision.

Online content

Any methods, additional references, Nature Portfolio reporting summaries, source data, extended data, supplementary information,

acknowledgements, peer review information; details of author contributions and competing interests; and statements of data and code availability are available at https://doi.org/10.1038/s41566-024-01456-5.

References

1. Taminiau, T., Stefani, F., Segerink, F. B. & Van Hulst, N. Optical antennas direct single-molecule emission. *Nat. Photon.* **2**, 234–237 (2008).
2. Liu, N., Tang, M. L., Hentschel, M., Giessen, H. & Alivisatos, A. P. Nanoantenna-enhanced gas sensing in a single tailored nanofocus. *Nat. Mater.* **10**, 631–636 (2011).
3. Sobhani, A. et al. Narrowband photodetection in the near-infrared with a plasmon-induced hot electron device. *Nat. Commun.* **4**, 1643 (2013).
4. Le Ru, E. C. & Etchegoin, P. G. Single-molecule surface-enhanced raman spectroscopy. *Ann. Rev. Phys. Chem.* **63**, 65–87 (2012).
5. Swearer, D. F. et al. Heterometallic antenna–reactor complexes for photocatalysis. *Proc. Natl Acad. Sci. USA* **113**, 8916–8920 (2016).
6. Novotny, L. & Hecht, B. *Principles of Nano-Optics* (Cambridge Univ. Press, 2012).
7. Knall, E. N. et al. Efficient source of shaped single photons based on an integrated diamond nanophotonic system. *Phys. Rev. Lett.* **129**, 053603 (2022).
8. Hepp, C. et al. Electronic structure of the silicon vacancy color center in diamond. *Phys. Rev. Lett.* **112**, 036405 (2014).
9. Jantzen, U. et al. Nanodiamonds carrying silicon-vacancy quantum emitters with almost lifetime-limited linewidths. *New J. Phys.* **18**, 073036 (2016).
10. Bhaskar, M. K. et al. Quantum nonlinear optics with a germanium-vacancy color center in a nanoscale diamond waveguide. *Phys. Rev. Lett.* **118**, 223603 (2017).
11. Trusheim, M. E. et al. Transform-limited photons from a coherent tin-vacancy spin in diamond. *Phys. Rev. Lett.* **124**, 023602 (2020).
12. Siyushev, P. et al. Optical and microwave control of germanium-vacancy center spins in diamond. *Phys. Rev. B* **96**, 081201 (2017).
13. Sipahigil, A. et al. An integrated diamond nanophotonics platform for quantum-optical networks. *Science* **354**, 847–850 (2016).
14. Guo, X. et al. Tunable and transferable diamond membranes for integrated quantum technologies. *Nano Lett.* **21**, 10392–10399 (2021).
15. Miller, O. D. et al. Fundamental limits to optical response in absorptive systems. *Opt. Express* **24**, 3329–3364 (2016).
16. Christiansen, R. E., Michon, J., Benzaouia, M., Sigmund, O. & Johnson, S. G. Inverse design of nanoparticles for enhanced raman scattering. *Opt. Express* **28**, 4444–4462 (2020).
17. Maity, S. et al. Spectral alignment of single-photon emitters in diamond using strain gradient. *Phys. Rev. Appl.* **10**, 024050 (2018).
18. Bergamin, M. et al. in *Quantum Information and Measurement* Th2C–6 (Optical Society of America, 2021).
19. Subedi, S., Fedorov, V., Mirov, S. & Markham, M. Spectroscopy of gr1 centers in synthetic diamonds. *Opt. Mater. Express* **11**, 757–765 (2021).
20. Baldwin Jr, J. A. Electron paramagnetic resonance investigation of the vacancy in diamond. *Phys. Rev. Lett.* **10**, 220 (1963).
21. Davies, G. Charge states of the vacancy in diamond. *Nature* **269**, 498–500 (1977).
22. Heremans, F., Fuchs, G., Wang, C., Hanson, R. & Awschalom, D. Generation and transport of photoexcited electrons in single-crystal diamond. *Appl. Phys. Lett.* **94**, 152102 (2009).
23. Wolfowicz, G. et al. Optical charge state control of spin defects in 4H-SiC. *Nat. Commun.* **8**, 1876 (2017).
24. Ohno, K. et al. Engineering shallow spins in diamond with nitrogen delta-doping. *Appl. Phys. Lett.* **101**, 082413 (2012).
25. Rugar, A. E. et al. Generation of tin-vacancy centers in diamond via shallow ion implantation and subsequent diamond overgrowth. *Nano Lett.* **20**, 1614–1619 (2020).
26. Tisler, J. et al. Highly efficient fret from a single nitrogen-vacancy center in nanodiamonds to a single organic molecule. *ACS Nano* **5**, 7893–7898 (2011).
27. Nelz, R. et al. Near-field energy transfer between a luminescent 2D material and color centers in diamond. *Adv. Quant. Technol.* **3**, 1900088 (2020).
28. Kong, X., Nir, E., Hamadani, K. & Weiss, S. Photobleaching pathways in single-molecule FRET experiments. *J. Am. Chem. Soc.* **129**, 4643–4654 (2007).
29. Roy, R., Hohng, S. & Ha, T. A practical guide to single-molecule FRET. *Nat. Methods* **5**, 507–516 (2008).
30. Novotny, L. & Van Hulst, N. Antennas for light. *Nat. Photon.* **5**, 83–90 (2011).
31. Michon, J., Benzaouia, M., Yao, W., Miller, O. D. & Johnson, S. G. Limits to surface-enhanced Raman scattering near arbitrary-shape scatterers. *Opt. Express* **27**, 35189–35202 (2019).
32. Mie, G. Beiträge zur optik trüber medien, speziell kolloidaler metallösungen. *Ann. Phys.* **330**, 377–445 (1908).
33. Neves, A. A. R., Cesar, C. L., Garbos, M. K., Euser, T. G. & Moreira, W. L. Expansion of arbitrary electromagnetic fields in terms of vector spherical wave functions. *Opt. Express* **24**, 2370–2382 (2016).
34. Chen, Y. et al. Ultralow-power cryogenic thermometry based on optical-transition broadening of a two-level system in diamond. *ACS Photon.* **10**, 2481–2487 (2023).
35. Feng, L. et al. Silver-coated elevated bowtie nanoantenna arrays: improving the near-field enhancement of gap cavities for highly active surface-enhanced Raman scattering. *Nano Res.* **8**, 3715–3724 (2015).
36. Fischer, H. & Martin, O. J. F. Engineering the optical response of plasmonic nanoantennas. *Opt. Express* **16**, 9144–9154 (2008).
37. Li, K., Stockman, M. I. & Bergman, D. J. Self-similar chain of metal nanospheres as an efficient nanolens. *Phys. Rev. Lett.* **91**, 227402 (2003).
38. Dengchao, H. et al. Metal–insulator–metal nanoislands with enhanced local fields for SERS-based detection. *ACS Appl. Nano Mater.* **18**, 16856–16863 (2023).
39. Michaels, A. M., Jiang, J. & Brus, L. Ag nanocrystal junctions as the site for surface-enhanced Raman scattering of single rhodamine 6G molecules. *J. Phys. Chem. B* **104**, 11965–11971 (2000).
40. Wang, P. et al. Transform-limited photon emission from a lead-vacancy center in diamond above 10 K. *Phys. Rev. Lett.* **132**, 073601 (2023).
41. Smith, J. M., Meynell, S. A., Bleszynski Jayich, A. C. & Meijer, J. Colour centre generation in diamond for quantum technologies. *Nanophotonics* **8**, 1889–1906 (2019).
42. McLellan, C. A. et al. Patterned formation of highly coherent nitrogen-vacancy centers using a focused electron irradiation technique. *Nano Lett.* **16**, 2450–2454 (2016).
43. Janitz, E., Bhaskar, M. K. & Childress, L. Cavity quantum electrodynamics with color centers in diamond. *Optica* **7**, 1232–1252 (2020).
44. Gottscholl, A. et al. Room temperature coherent control of spin defects in hexagonal boron nitride. *Sci. Adv.* **7**, eabf3630 (2021).
45. Anderson, C. P. et al. Five-second coherence of a single spin with single-shot readout in silicon carbide. *Sci. Adv.* **8**, eabm5912 (2022).
46. Zhong, T., Kindem, J. M., Miyazono, E. & Faraon, A. Nanophotonic coherent light–matter interfaces based on rare-earth-doped crystals. *Nat. Commun.* **6**, 8206 (2015).

47. Bayliss, S. et al. Enhancing spin coherence in optically addressable molecular qubits through host-matrix control. *Phys. Rev. X* **12**, 031028 (2022).
48. Moerner, W. E. & Kador, L. Optical detection and spectroscopy of single molecules in a solid. *Phys. Rev. Lett.* **62**, 2535 (1989).
49. Diez, D. M., Barr, C. D. & Cetinkaya-Rundel, M. *OpenIntro Statistics* (OpenIntro Boston, 2012).
50. Fan, X., Zheng, W. & Singh, D. J. Light scattering and surface plasmons on small spherical particles. *Light Sci. Appl.* **3**, e179–e179 (2014).
51. Alaee, R., Rockstuhl, C. & Fernandez-Corbaton, I. Exact multipolar decompositions with applications in nanophotonics. *Adv. Opt. Mater.* **7**, 1800783 (2019).

Methods

Sample preparation

We use diamond membranes for this work due to their higher vacancy density, but we observe the same phenomena in bulk diamonds too. Nanoscale-thick uniform diamond membranes were synthesized via smart-cut[52] and isotopically (^{12}C) purified via plasma-enhanced chemical vapour deposition overgrowth[24]. GeVs were synthesized via ion implantation followed by a multi-step annealing process. The membranes were then lithographically patterned into 200 μm × 200 μm squares and transferred onto hydrogen silsesquioxane-coated fused-silica wafers[14].

Optical measurement

For the PLE measurements of the GeVs, the probe laser is generated by a wave-mixing module (AdvR) combining a tunable continuous-wave Ti:sapphire laser (M Squared Solstis) and a monochromatic continuous-wave laser in telecommunication band (Thorlabs, SFL 1550P). We use this laser system, composed of frequency steps of 150 MHz with 20 ms dwell time at each step, to scan across the GeV's ZPL and collect the emission from phonon sidebands through double filters (2× Semrock FF01-647/57-25). For off-resonant pump measurements, the pump is realized using a 633 nm diode laser, with an optical beam shutter (Thorlabs, SH05R) to switch it on and off. In the calculation of resonant fluence, we incorporate a combined function of laser power, scanning speed, and the lineshape of the GeV. Specifically, we model the GeV spectral density as a Lorentzian lineshape peaked at the resonant frequency. At each frequency point in the scan, the effective laser fluence delivered to the GeV is estimated as the product of power, dwell time, and spectral density. The total fluence is then obtained by summing the laser fluence over all frequencies in the scan. For off-resonant pump fluence (fixed frequency), we simply multiply the pump power by the fixed pump duration of 5 s. All of the PLE measurements are taken at 4 K in a closed-loop cryostation (Montana S200).

DFT calculation

We performed DFT calculations to determine the Stark shift of the ZPL of the negatively charged GeV in diamond. All calculations used the semi-local Perdew–Burke–Ernzerhof functional[53] and the Quantum Espresso code[54,55]. We used a (3 × 3 × 3) supercell containing 214 carbon atoms and one germanium atom, with the Brillouin zone sampled at the Γ-point, SG15-optimized norm-conserving Vanderbilt pseudopotentials[56,57], and a plane-wave basis set with a kinetic energy cut-off of 90 Rydberg. We used a diamond lattice constant of 3.568 Å, which was converged for 90 Rydberg. The energy of the ZPL was approximated as the adiabatic excitation energy of the first excited state, which was investigated using the constrained occupations DFT (ΔSCF); see Supplementary Sections 3 and 4 for more details.

Data availability

The datasets generated and/or analysed during the current study are available from the corresponding author on reasonable request.

References

52. Aharonovich, I. et al. Homoepitaxial growth of single crystal diamond membranes for quantum information processing. *Adv. Mater.* **24**, OP54–OP59 (2012).
53. Perdew, J. P., Burke, K. & Ernzerhof, M. Generalized gradient approximation made simple. *Phys. Rev. Lett.* **77**, 3865 (1996).
54. Giannozzi, P. et al. Quantum espresso: a modular and open-source software project for quantum simulations of materials. *J. Phys. Condens. Matter* **21**, 395502 (2009).
55. Giannozzi, P. et al. Quantum espresso toward the exascale. *J. Chem. Phys.* **152**, 154105 (2020).
56. Hamann, D. Optimized norm-conserving Vanderbilt pseudopotentials. *Phys. Rev. B* **88**, 085117 (2013).
57. Schlipf, M. & Gygi, F. Optimization algorithm for the generation of oncv pseudopotentials. *Comput. Phys. Commun.* **196**, 36–44 (2015).

Acknowledgements

We acknowledge funding from Q-NEXT, supported by the US Department of Energy, Office of Science, National Quantum Information Science Research Centers. Z.L. acknowledges support from the Kadanoff-Rice fellowship (grant no. NSF DMR-2011854). Diamond growth-related efforts were supported by the US Department of Energy, Office of Basic Energy Sciences, Materials Science and Engineering Division (N.D.). The membrane bonding work is supported by NSF award no. AM-2240399. This work made use of the Pritzker Nanofabrication Facility (Soft and Hybrid Nanotechnology Experimental Resource, NSF award no. ECCS-2025633) and the Materials Research Science and Engineering Center (NSF award no. DMR-2011854) at the University of Chicago. F.A. acknowledges support from the ICFOstepstone—PhD Programme funded by the European Union's Horizon 2020 Research and Innovation programme under Marie Skłodowska-Curie grant agreement no. 713729. D.C. acknowledges support from the European Union's Horizon 2020 Research and Innovation programme, under European Research Council grant agreement no. 101002107 (NEWSPIN); the Government of Spain (Severo Ochoa grant no. CEX2019-000910-S); Generalitat de Catalunya (CERCA program and AGAUR project no. 2021 SGR 01442); and Fundació Cellex and Fundació Mir-Puig. First-principles calculations were performed in the MICCoM center—a computational materials science centre funded by the US Department of Energy, Office of Basic Energy Sciences, and used resources of the University of Chicago Research Computing Center.

Author contributions

Z.L. and X.G. performed the experiments and analysed the data. Y.J. and A.B. performed first-principles calculations under the supervision of G.G. F.A. performed near-field calculations under the supervision of D.C. D.D.A., N.D. and F.J.H. provided the materials. A.A.H. conceived and supervised the project. All authors discussed the results and contributed to the paper.

Competing interests

The authors declare no competing interests.

Additional information

Supplementary information The online version contains supplementary material available at https://doi.org/10.1038/s41566-024-01456-5.

Correspondence and requests for materials should be addressed to Alexander A. High.

Peer review information *Nature Photonics* thanks the anonymous reviewers for their contribution to the peer review of this work.